Applied Surface Science 505 (2020) 144551

Contents lists available at ScienceDirect

Applied Surface Science

journal homepage: www.elsevier.com/locate/apsusc

Full Length Article

Elucidating the mechanism for the chemical vapor deposition growth of vertical MoO_2/MoS_2 flakes toward photoelectrochemical applications

Tran Nam Trung[a,b], Fadi Z. Kamand[a], T.M. Al tahtamouni[a,*]

[a] Materials Science & Technology Program, College of Arts & Sciences, Qatar University, Doha 2713, Qatar
[b] Department of Physics & Materials Science, Faculty of Natural Sciences, Quy Nhon University, Quy Nhon 590000, Viet Nam

ARTICLE INFO

Keywords:
Growth mechanism
Vertically aligned flakes
MoO_2/MoS_2 heterostructure
Chemical vapor deposition
Photoelectrochemical water splitting

ABSTRACT

To control the growth of layered two-dimensional transition metal dichalcogenide (TMD) materials or complex structures such as heterostructures, it is important to understand the growth mechanism. In this study, we demonstrated the chemical vapor deposition (CVD) growth of vertically aligned MoO_2/MoS_2 flakes by using sulfur and molybdenum trioxide (MoO_3) powders as precursors. Moreover, based on various experimental measurements, a detailed growth mechanism is proposed for elucidating the conversion of MoO_2 to MoS_2 in the CVD process to achieve vertically aligned MoO_2/MoS_2 flakes. Our results reveal that two competing pathways for sulfurization reactions occur during the CVD growth process: the dominance of the reactions in the vapor-phase pathway facilitates the formation of parallel-aligned MoS_2 flakes, while the dominance of the reactions in the solid-phase pathway determines the formation of vertically aligned MoO_2/MoS_2 flakes. In addition, the photoelectrochemical (PEC) activity of the vertically aligned MoO_2/MoS_2 flakes was evaluated for hydrogen production applications based on PEC water splitting. Our results open the door to promote the process for designing the growth of other TMD materials or complex structures, which can be beneficial for use in various applications.

1. Introduction

Owing to their unique electronic, physical, chemical and mechanical properties, transition metal oxides (TMOs) and transition metal dichalcogenides (TMDs) have been considered as functional materials for realizing future applications in nanotechnology. The use of two-dimensional (2D) layered TMDs for a broad range of applications in electronics, optoelectronics, batteries, electrocatalysis and photoelectrocatalysis has recently attracted much attention, and molybdenum disulfide (MoS_2) is one of the most prominent candidate materials [1–3]. As analogous to the structure of graphene, intralayers of MoS_2 are composed of sandwiched layers of Mo and S arranged in a hexagonal geometry with strong covalent bonds, while interlayers of MoS_2 are held together by weak Van de Waals interactions [4,5]. Interestingly, MoS_2 exhibits tunable bandgaps from ~1.2 eV for the indirect gap of the bulk form to ~1.9 eV for the direct gap of the monolayer [4,6]. It is widely believed that MoS_2 in the bulk form has poor catalytic activity due to the lack of catalytically active sites. Both theoretical and experimental studies have pointed out that the strong catalytic activity of MoS_2 nanostructures arises from active S atom sites that are exposed along the edges [7,8]. However, the relatively low interlayer conductivity of MoS_2 nanostructures has limited its catalytic applications in electrocatalytic and photoelectrocatalytic devices for hydrogen production [9]. Therefore, extensive efforts have been devoted to acquire favorable morphologies of MoS_2 with abundant active edge sites such as nanoflakes and nanosheets as well as to improve conductivity by coupling with other materials, such as graphene, TiO_2, ZnO, MoO_2, etc., to name just a few [9–11].

MoO_2 is a member of a family of metallic TMOs with a high conductivity. MoO_2 has been identified as a promising catalyst for energy storage and energy conversion applications [12,13]. In recent years, hybrid MoO_2/MoS_2 nanostructures have gained enormous research interest as catalytic materials for electrochemical applications. For instance, Xiao *et al.* [14] fabricated nanocarved MoO_2/MoS_2 hybrids by using in situ grown MoS_2 as nanomasks with control of the morphology and hybridization of the molybdenum compounds. The hybrid structure has been found to synergistically enhance the electrochemical performance of MoO_2 and MoS_2, especially at high current rates. Rheem *et al.* [15] synthesized MoS_2 nanosheets on MoO_2 nanofibers by electrospinning followed by a postheat treatment process. A greatly enhanced electrocatalytic hydrogen evolution reaction performance was observed for the hierarchical MoO_2/MoS_2 nanostructures, which was explained

* Corresponding author.
E-mail address: taltahtamouni@qu.edu.qa (T.M. Al tahtamouni).

https://doi.org/10.1016/j.apsusc.2019.144551
Received 29 August 2019; Received in revised form 18 October 2019; Accepted 30 October 2019
Available online 05 November 2019

by an improved conductivity of the catalyst and by an increased number of active edge sites. Most recently, Yan *et al.* [16] prepared nanoflowers/nanoflakes MoS_2/MoO_2 heterostructures on porous carbon paper by direct chemical vapor deposition (CVD) growth for electrochemical hydrogen production. They concluded that MoS_2 by itself does not exhibit much activity, while the apparent hydrogen evolution reaction performance was attributed to the incorporation of MoO_2 impurities/composites. Despite the efforts put into the synthesis of hybrid MoO_2/MoS_2 nanostructures for enhancing electrochemical performance, relatively little attention, however, has been spent on studies aimed at understanding the growth mechanism and for capturing the transformation of MoO_2 to MoS_2 to achieve vertical MoO_2/MoS_2 flakes.

In this study, we report on our recent efforts in understanding the mechanism behind the formation of vertical MoO_2/MoS_2 flakes during the CVD growth process. By varying the sulfur concentration in the presence of MoO_3 powder used as a molybdenum precursor, we obtained MoO_2/MoS_2 flakes with different morphologies. Based on our experimental results, sulfurization reactions that occur via two pathways: vapor-phase pathway and solid-phase pathway are proposed for unraveling the conversion of MoO_2 to MoS_2. The dominance of the reactions in the vapor-phase pathway facilitates the formation of parallel-aligned MoS_2 flakes, while the dominance of the reactions in the solid-phase pathway determines the formation of vertically aligned MoO_2/MoS_2 flakes. In addition, MoO_2/MoS_2 flakes deposited on TiO_2 nanorod arrays were used as photoelectrodes in photoelectrochemical (PEC) cells to test the PEC water splitting performance for hydrogen production.

2. Experimental section

The growth of MoO_2/MoS_2 flakes was carried out in a Lindberg Blue M CVD system with a tubular furnace and a 2-inch diameter quartz tube. A Si wafer coated with 300 nm SiO_2 (Si/SiO_2) was used as a substrate for the growth of MoO_2/MoS_2. Prior to the growth, substrates were successively cleaned for 15 min in acetone, methanol and deionized (DI) water in an ultrasonic bath, and then dried under nitrogen flow. High-purity molybdenum trioxide (MoO_3) powder (99.97%, Sigma Aldrich) and sulfur powder (99.5%, Sigma Aldrich) were used as precursors. High-purity argon (Ar, 99.999%) was used as a carrier gas. MoO_3 precursor was placed into a 10 cm-long alumina ceramic boats, while sulfur powder was placed into another ceramic crucible. For a typical growth, the substrates were placed with their surface facing downwards on top of a ceramic boat containing 20 mg of MoO_3 powder. The MoO_3 boat with the mounted substrates was kept at the center of the furnace, while the ceramic crucible containing 200 mg of sulfur powder was held upstream at a distance of 15 cm from the MoO_3 boat. The temperature of the MoO_3 boat and sulfur crucible was monitored by two separate thermocouples. A schematic of the experimental setup is shown in Fig. S1 (see Supporting Information). After evacuation of the reactor, the quartz tube was purged with 100 sccm (standard cubic centimeter per minute) Ar flow for 15 min. The furnace was then heated to 700 °C at a temperature ramp rate of 15 °C/min under 100 sccm Ar flow and held at this set point for 20 min. At this stage, the temperature of the sulfur crucible reached 180 °C. After deposition, the furnace was naturally cooled down while maintaining the 100 sccm Ar flow. When the temperature of the furnace was cooled down to 450 °C, the Ar flow rate was increased to 500 sccm for rapid cooling down of the system and for removing residual byproducts.

TiO_2 nanorods on a fluorine-doped tin oxide (FTO) glass substrate were synthesized using a hydrothermal method. A mixture solution of 15 ml deionized (DI) water, 15 ml HCl and 0.3 ml titanium butoxide ($C_{16}H_{36}O_4Ti$) was placed into a Teflon-lined stainless-steel autoclave and heated at 160 °C for 10 h. Postsynthesis, the TiO_2 nanorod substrates were rinsed several times in DI water and then dried under nitrogen gas flow. MoO_2/MoS_2 flakes were synthesized on the TiO_2 nanorod substrates at 700 °C for 20 min with the use of 20 mg MoO_3 and 200 mg sulfur powders.

A scanning electron microscope (SEM, Nova Nano 450) and transmission electron microscope (TEM, FEI Talos F200X) were used to visualize the morphologies and microstructures of the samples. Raman spectra for the samples were obtained at room temperature using a Thermo Fisher Scientific (DXR™ 2 Smart) Raman microscope with a laser excitation line of 532 nm. The 6 mW-power of the excitation laser was focused to a spot size of ~0.7 μm with a 50× objective lens. The Raman signals were collected using a 900 lines/mm grating by a charge-coupled device (CCD) detector. X-ray photoelectron spectroscopy (XPS, AXIS Ultra DLD) was used to determine the chemical states and binding energies of the deposited structures.

The PEC measurements were performed in 1 M KOH electrolyte solution using a three-electrode configuration. A Pt coin and KCl-saturated calomel (Hg/Hg_2Cl_2) were used as counter and reference electrodes, respectively. The TiO_2 nanorod substrates and $TiO_2/MoO_2/MoS_2$ flake substrates were used as working electrodes (photoelectrodes) with a working area of 0.5 × 0.5 cm^2. The PEC performance of the TiO_2 and $TiO_2/MoO_2/MoS_2$ photoelectrodes was evaluated by recording linear sweep voltammetry (LSV) and chronoamperometry ($I-t$) using a Gamry interface 1010E potentiostat and a 150 W Xe arc solar simulator with an AM 1.5 G filter as the light source.

3. Results and discussion

The sulfur concentration in the CVD growth process was controlled by supplying different amounts of the sulfur precursor. This implies that a larger amount of sulfur powder produces a higher concentration of sulfur vapor during the CVD process. Fig. 1 shows the SEM images of samples grown by using different amounts of supplied sulfur: 100 mg, 200 mg, 300 mg and 400 mg, which are hereafter referred to as samples S1, S2, S3 and S4, respectively. For sample S1 with a low sulfur amount of 100 mg, highly dense and thick vertical flakes with a size of ~1 μm were formed, as seen in Fig. 1(a). As the sulfur amount increases to 200 mg, the density of the film becomes lower, while the thickness of the vertical flakes becomes thinner, as observed in the SEM image of sample S2 (Fig. 1(b)). Further increasing the amount of sulfur powder to 300 mg results in a significant change in the morphology of sample S3, in which, along with the vertically aligned flakes, other parallel-aligned nanostructures marked by yellow dotted circles are observed, as seen in Fig. 1(c). Due to the smaller size (~500 nm) of the flakes in sample S3, the density of the film is also lower in comparison to samples S1 and S2. At a higher sulfur amount of 400 mg, the orientation of the flakes in sample S4 was totally changed to a parallel alignment with the substrate surface, as shown in Fig. 1(d). Based on the SEM results, it is clearly indicated that upon increasing the sulfur concentration, the morphologies of the samples tend to change from vertically aligned flakes to parallel-aligned flakes.

To examine the structural properties as well as the imprints of other possible phases in the samples, Raman spectra were recorded, as shown in Fig. 2. All the samples showed two distinct MoS_2 Raman peaks positioned near 400 cm^{-1} (denoted by black square (■) signs), corresponding to the in-plane E^1_{2g} mode due to the vibration of Mo and S atoms, and the out-of-plane A_{1g} mode due to the vibration of S atoms [4,6]. However, the spectra for samples S1 and S2 exhibit additional Raman peaks (denoted by black dot (●) signs) corresponding to the imprint of the MoO_2 phase [14,17]. It was determined that, upon increasing the amount of sulfur powder from sample S1 to sample S2, the intensity of the Raman peaks decrease and increase for the MoO_2 and MoS_2 phases, respectively. This implies that the MoO_2 phase is gradually converted to the MoS_2 phase in sample S2 in comparison with sample S1. With a further increase in sulfur amount, the Raman peaks due to the MoS_2 phase are dominant in samples S3 and S4, whereas the Raman peaks due to the MoO_2 phase disappear, as clearly seen in the short-range Raman spectra measured for these samples (inset in Fig. 2).

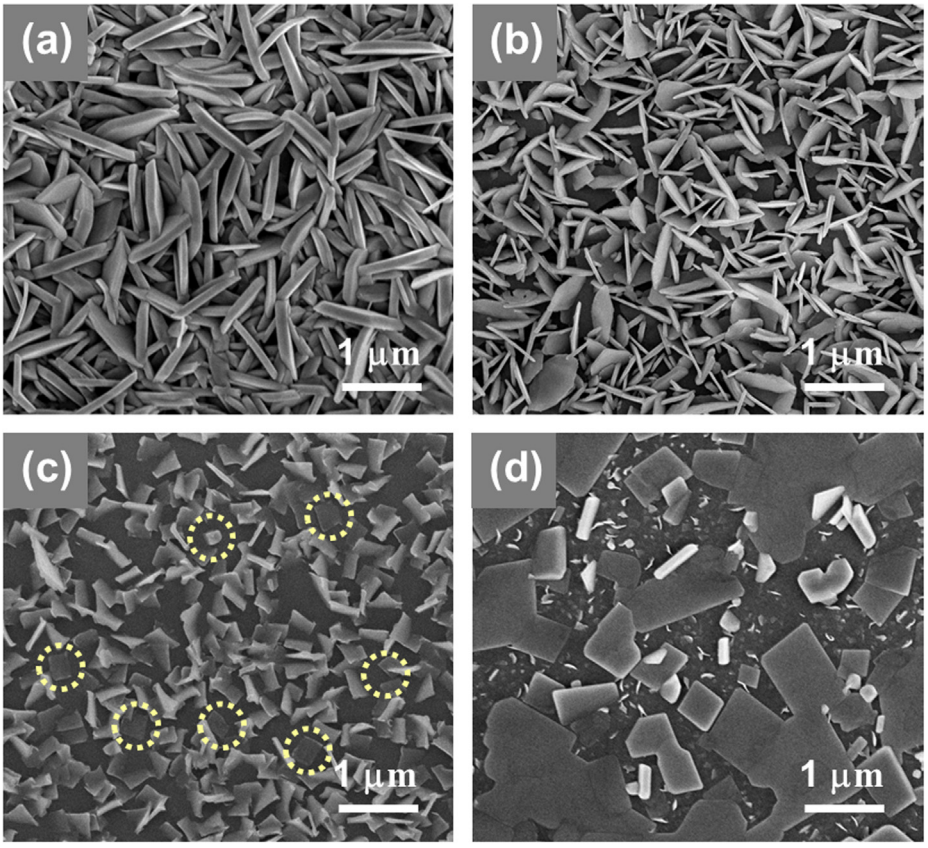

Fig. 1. SEM images of samples (a) S1, (b) S2, (c) S3 and (d) S4, which were grown using different amounts of sulfur.

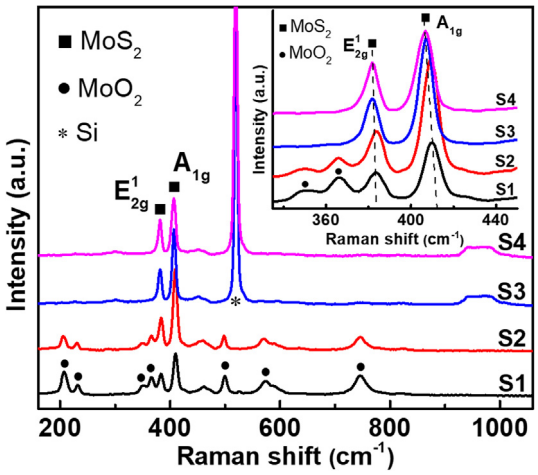

Fig. 2. Raman spectra for samples S1, S2, S3 and S4. The Raman modes for MoS_2, MoO_2 and Si were marked with square (■), dot (●) and asterisk (*) signs, respectively. The inset shows the short-range Raman spectra, which clearly show the positions of the E^1_{2g} and A_{1g} Raman modes.

This finding indicates a phase conversion from MoO_2 into MoS_2 on the sample surface.

TEM measurements were carried out to explore the microstructure of the vertically aligned flakes. Fig. 3(a) shows a representative TEM image with a low-magnification of the sample in which the flake structure with a size of ~ 150 nm can be clearly seen. The high-resolution TEM image in Fig. 3(b), which was captured at the area marked with a white dashed line in Fig. 3(a), reveals that the flake contains two different fringe patterns. The outer shell shows a lattice spacing of ~ 0.62 nm, which corresponds to the (0 0 2) crystal plane of hexagonal MoS_2 [18]. The lattice fringe of the inner core is ~ 0.34 nm, which is in good agreement with the (0 1 1) crystal plane of MoO_2, as reported previously [10,14]. Moreover, for a better understanding of the chemical composition of the flakes, X-ray energy dispersive spectroscopy (EDS) mapping was performed, as shown in Fig. 3(c). It is confirmed that the flakes are mostly composed of molybdenum (Mo), sulfur (S) and oxygen (O) elements, in which the Mo and S elements are homogeneously distributed throughout the whole flakes, while an inhomogeneous distribution of the O element is observed. Given these results, it can be concluded that the vertically aligned flakes have a core/shell MoO_2/MoS_2 structure, which is composed of two phases: MoO_2 in the inner core and MoS_2 in the outer shell.

To further determine the elements and chemical state of the vertically aligned MoO_2/MoS_2 flakes, XPS analysis was employed, as shown in Fig. 4. The survey spectrum in Fig. 4(a) evidently reveals the presence of Mo, O and S elements. By deconvoluting the Mo 3d peaks in Fig. 4(b) using the fitted Gaussian curves, two separate overlapping doublet peaks are clearly observed. These doublet peaks are attributed to Mo $3d_{5/2}$ and Mo $3d_{3/2}$ for the Mo^{4+} oxidation states. The doublet peaks at binding energies of 228.5 eV (Mo $3d_{5/2}$) and 231.7 eV (Mo $3d_{3/2}$) belong to the Mo^{4+} oxidation state in the pure MoS_2 crystal [19], while the doublet peaks at binding energies of 229.5 eV (Mo $3d_{5/2}$) and 233.5 eV (Mo $3d_{3/2}$) belong to the Mo^{4+} oxidation state in MoO_2 [20,21]. Along with the Mo3d peaks, a peak appears at 226.1 eV, which is associated with the S 2 s component in elemental sulfur (Fig. 4(b)) [19]. The S 2p peaks in Fig. 4(c) are deconvoluted into three peaks. A doublet peak at binding energies of 161.4 eV and 162.5 eV is ascribed to S $2p_{3/2}$ and S $2p_{1/2}$ for the S 2p component, which is attributed to the S–Mo bonds in the basal plane of MoS_2 [22]. The peak positioned at 163.6 eV may be attributed to the thiomolybdate (Mo_xS_y) species, which is formed due to anion vacancies in the MoS_2 crystal lattice [23]. Moreover, the O 1 s peak positioned at 531.8 eV, as observed in Fig. 4(d), verifies the presence of the O^{2-} oxidation state in MoO_2 [24].

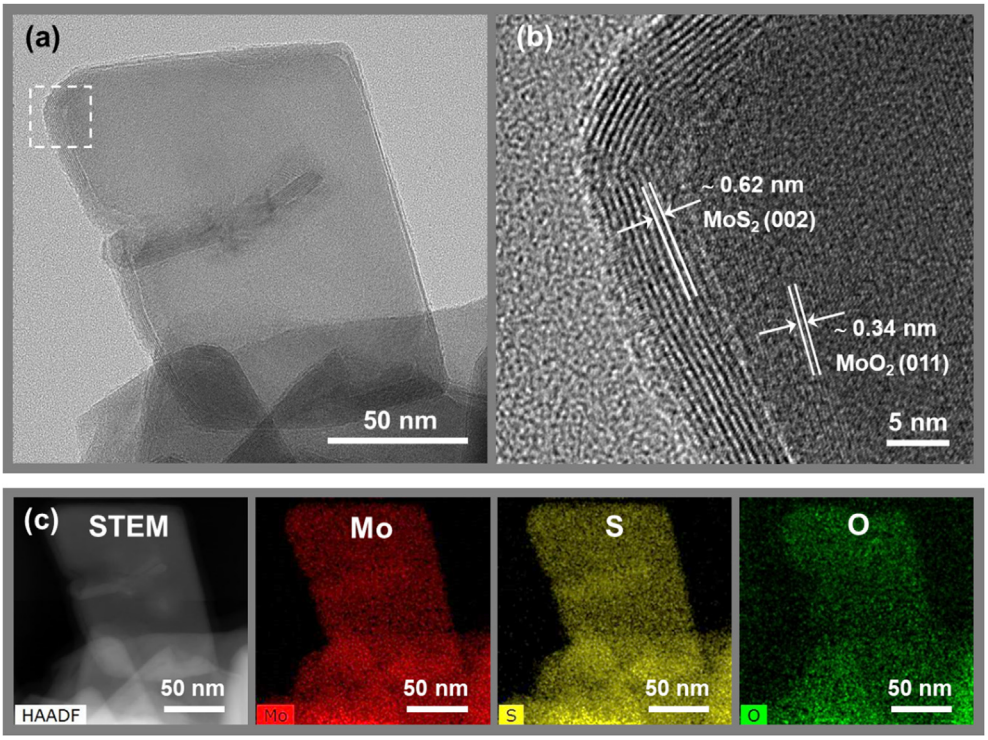

Fig. 3. (a) Low- and (b) high-magnification TEM images of the vertical MoO_2/MoS_2 flakes. (c) EDS elemental mapping of Mo, S and O for the vertical flakes.

The peak positioned at 528.6 eV may be ascribed to the strongly absorbed oxygen (O^-) OH^- group [9].

The well-known sulfurization reaction in the CVD synthesis of MoS_2 using elemental sulfur (S) and molybdenum trioxide (MoO_3) powder is presented in Eq. (1), which can be described by intermediate reactions (2) and (3), as follows [25,26]:

$$2\ MoO_{3\ |\ (g)} + 7\ S_{(g)} \rightarrow 2\ MoS_{2\ |\ (s)} + 3\ SO_{2\ |\ (g)} \quad (1)$$

$$2\ MoO_3 + S \rightarrow 2\ MoO_2 + SO_2 \quad (2)$$

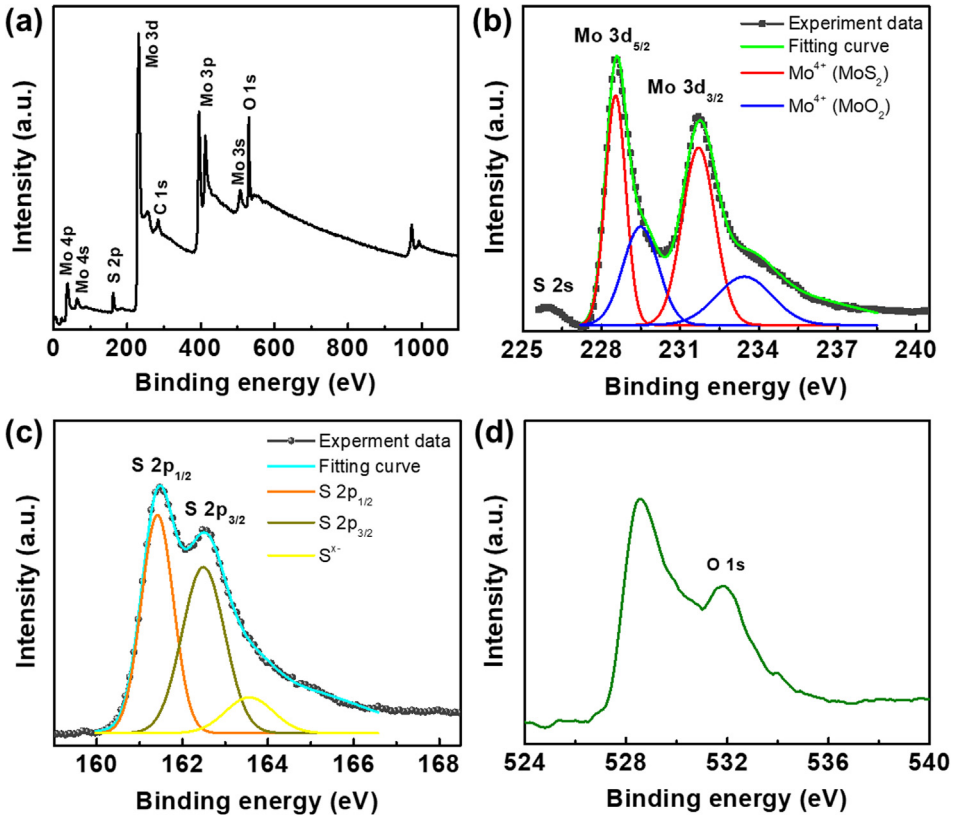

Fig. 4. XPS spectra for the (a) survey, (b) Mo 3d, (c) S 2p and (d) O 1 s core-levels of the vertically aligned MoO_2/MoS_2 flake sample.

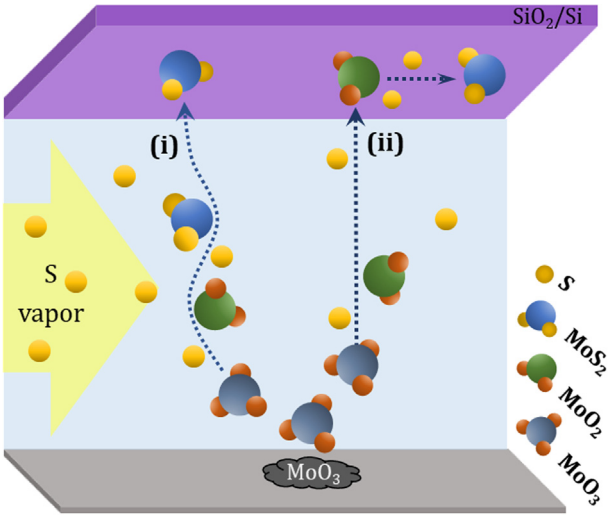

Fig. 5. Schematic showing the growth mechanism in the CVD process with two competing reaction pathways: (i) vapor-phase pathway and (ii) solid-phase pathway.

$$2\ MoO_2 + 6\ S \rightarrow 2\ MoS_2 + 2\ SO_2 \quad (3)$$

In reaction (2), under a sulfur vapor environment, MoO_3 is partially reduced to form the intermediated MoO_2. Then, in reaction (3), the intermediated MoO_2 further reacts with sulfur vapor to form MoS_2 by the substitution of oxygen by sulfur. However, the reaction pathways for the conversion of MoO_2 to MoS_2 and for the formation of the MoO_2/MoS_2 structure have yet to be fully understood.

Based on our experimental results, it is proposed that the sulfurization reactions between intermediated MoO_2 and sulfur vapor possibly occur in two pathways, as sketched in Fig. 5. There are two competing pathways for the reactions: (i) the vapor-phase pathway by direct reaction, and (ii) the solid-phase pathway by absorption and diffusion. In pathway (i), the intermediated MoO_2 directly reacts with sulfur vapor to completely form MoS_2, which is then subsequently deposited onto the substrate as MoS_2 clusters with further growth to MoS_2 nanostructures. In terms of growth rate, this pathway is considered to be a slow process because it needs sufficient time to complete the conversion reactions of MoO_2 into MoS_2 in the gas phase before reaching the substrate. In fact, slowing down the reaction rate will facilitate the formation of the parallel-aligned nanostructures of MoS_2 [27]. In pathway (ii), after the absorption and diffusion of the intermediated MoO_2 onto the surface of the substrate, MoO_2 clusters are formed on the substrate. The MoO_2 clusters serve as feeding sites for other molecular MoO_2 growth. As a result, the growth rate for these sites becomes fast due to a matching in the structure of the feeding sites of MoO_2 and the incoming molecular MoO_2. Under such a fast process, incoming molecular MoO_2 is favorably deposited along the edges of the clusters due to their high surface energy [28], resulting in the formation of vertically aligned nanostructures. During this process, the sulfur vapor will diffuse onto the surface of the MoO_2 nanostructures, react and then convert the top layers of MoO_2 into MoS_2 [29]. As a result, the MoO_2/MoS_2 heterostructures are formed. In fact, it is difficult to determine the priority as well as separate the controlling factors of each pathway. However, the pathways may compete directly with each other during the growth process, which could be affected by the growth parameters such as concentration of reactant precursors, reaction duration and processing temperature.

As assumed above, the slow- and fast-processes for the growth rate are favorable for the growth of parallel and vertically aligned nanostructures, respectively. It is found that the sulfur concentration plays a crucial role in the formation and orientation of nanostructures during the CVD process. In an excess sulfur environment, most of the MoO_2 is surrounded by plenty of reducing species (sulfur vapor), making the reaction in the vapor-phase pathway (pathway (i)) dominant. Thereby, the formation of the parallel-aligned MoS_2 flakes is a consequence of the slow process. This is the case for sample S4, as observed in Fig. 1(d). Whereas under the sulfur deficient environment, the formation of MoS_2 via direct reaction in the vapor-phase pathway is impeded due to the poor reducing atmosphere, while the reaction in the solid-phase pathway (pathway (ii)) is dominant. As a result of the fast process, the vertically aligned MoO_2/MoS_2 flakes are formed. This is the case for samples S1 and S2, as observed in Fig. 1(a) and (b). However, both phases of MoO_2 and MoS_2 coexist at the same time, as confirmed by the Raman spectra shown in Fig. 2. The detection of two coexisting phases in these samples can be explained by the encapsulation of MoO_2 with the outer shell of MoS_2 due to the conversion of the top layer of MoO_2 to MoS_2 by the diffusion of sulfur species. This conversion takes place at the interface of MoO_2 and MoS_2, and it will limit the diffusion of sulfur species through the already formed MoS_2 outer shell [29].

To evaluate the photoelectrochemical activity of the vertically aligned MoO_2/MoS_2 flakes, we conducted the growth of MoO_2/MoS_2 flakes on TiO_2 nanorods to form TiO_2/MoO_2/MoS_2 heterostructures. The detailed information for the growth of TiO_2 nanorods and TiO_2/MoO_2/MoS_2 heterostructures is addressed in the experimental section. To prepare PEC cells, the synthesized TiO_2/MoO_2/MoS_2 photoelectrode, hereafter referred to as the TM photoelectrode, was prepared with a working area of $0.5 \times 0.5\ cm^2$ using nonconductive epoxy to cover the undesired area. A photoelectrode composed of TiO_2 nanorods with the same working area was also prepared as a counterpart. It is shown that there is a small difference in the current density–voltage (J–V) curves measured for the TiO_2 photoelectrode in the dark and under illumination, as shown in Fig. 6(a). This can be explained by the low yield for light harvesting for TiO_2, which has a large band gap of ~ 3.03 eV and so only absorbs light in the ultraviolet regime. The TM photoelectrode exhibited a significantly higher photocurrent (0.6 mA/cm^2 at 0.4 V) compared to the TiO_2 counterpart (0.03 mA/cm^2 at 0.4 V). This enhancement can be understood by combining the advantages of the vertical MoO_2/MoS_2 flakes as well as the advantages of the heterostructure. The vertical MoO_2/MoS_2 flakes have large specific surface areas with high catalytic active sites, while the heterostructure has the benefit of effective separation of photogenerated electrons and holes to the proper electrodes (see Fig. S2 in Supporting Information) due to a suitable band gap (1.86 and 3.03 eV) and electron affinities (4.0 and 4.8 eV) for MoS_2 and TiO_2, respectively [30]. The chronoamperometry recorded at 0.4 V in Fig. 6(b) again confirmed the enhanced performance of the TM photoelectrode, where it exhibits a photocurrent density that is 20 times higher than that of the TiO_2 photoelectrode. Additionally, the photocurrent of the TM photoelectrode did not change over 500 s of illumination, suggesting the effective separation of photogenerated charges as well as the stability of the TM photoelectrode. Thus, we believe that the PEC performance of our samples could be further improved by manipulating the morphologies of the vertically aligned MoO_2/MoS_2 flakes during the CVD process, which will be explored for fabricating effective photoelectrodes for efficient hydrogen production in the future.

4. Conclusion

In summary, vertically aligned MoO_2/MoS_2 flakes were synthesized using a CVD approach with sulfur and MoO_3 powder precursors. Based on various experimental measurements, the growth mechanism for the vertically aligned flakes was investigated in detail, for which two competing pathways for sulfurization reactions in the vapor- and solid-phases were proposed. The dominance of the reactions in the vapor-phase pathway, which corresponds to an excess sulfur environment, facilitated the formation of parallel-aligned MoS_2 flakes. However, the dominance of the reactions in the solid-phase pathway, which corresponds to a sulfur deficient environment, generated vertically aligned

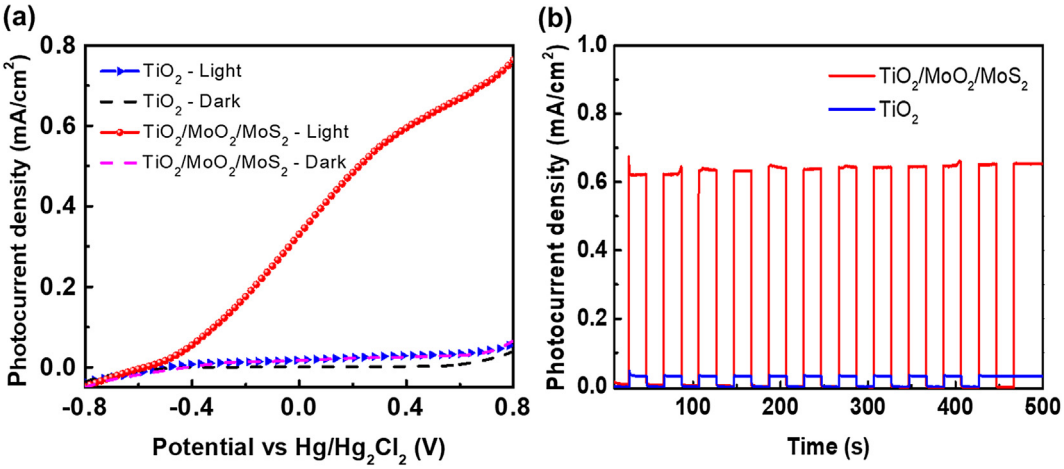

Fig. 6. (a) Linear sweep voltammetry curves for TiO_2 and $TiO_2/MoO_2/MoS_2$ photoelectrodes in the dark and under light illumination. (b) Chronoamperometry for the TiO_2 and $TiO_2/MoO_2/MoS_2$ photoelectrodes at an applied voltage of 0.4 V vs. Hg/Hg_2Cl_2.

MoO_2/MoS_2 flakes. Moreover, the photoelectrochemical activity of the vertically aligned MoO_2/MoS_2 flakes was evaluated for hydrogen production based on PEC water splitting, in which the TM heterostructure photoelectrode showed a significantly enhanced performance (20 times higher) in comparison to the bare TiO_2 photoelectrode. Our results imply that understanding of the growth mechanism is necessary to promote the process of designing the growth of other TMD materials or complex structures such as heterostructures, which can be beneficial in various applications such as batteries, catalysis, and electrochemical and photoelectrochemical hydrogen production.

Declaration of Competing Interest

The authors declare that they have no known competing financial interests or personal relationships that could have appeared to influence the work reported in this paper.

Acknowledgements

This research is supported by a grant from Qatar University under Grant Number GCC-2017-007. The authors are thankful to QEERI Core Labs for TEM measurements.

Appendix A. Supplementary material

Supplementary data to this article can be found online at https://doi.org/10.1016/j.apsusc.2019.144551.

References

[1] Q. Ji, Y. Zhang, T. Gao, Y. Zhang, D. Ma, M. Liu, Y. Chen, X. Qiao, P.-H. Tan, M. Kan, J. Feng, Q. Sun, Z. Liu, Epitaxial monolayer MoS2 on mica with novel photoluminescence, Nano Lett. 13 (8) (2013) 3870–3877.
[2] Y. Li, H. Wang, L. Xie, Y. Liang, G. Hong, H. Dai, MoS2 nanoparticles grown on graphene: an advanced catalyst for the hydrogen evolution reaction, J. Am. Chem. Soc. 133 (19) (2011) 7296–7299.
[3] Q.H. Wang, K. Kalantar-Zadeh, A. Kis, J.N. Coleman, M.S. Strano, Electronics and optoelectronics of two-dimensional transition metal dichalcogenides, Nat. Nanotechnol. 7 (2012) 699.
[4] L. Hong, Z. Qing, Y.C.C. Ray, T.B. Kang, E.T.H. Tong, O. Aurelien, B. Dominique, From bulk to monolayer MoS2: evolution of Raman scattering, Adv. Funct. Mater. 22 (7) (2012) 1385–1390.
[5] C. Lee, H. Yan, L.E. Brus, T.F. Heinz, J. Hone, S. Ryu, Anomalous lattice vibrations of single- and few-layer MoS2, ACS Nano 4 (5) (2010) 2695–2700.
[6] T.N. Trung, D.-B. Seo, N.D. Quang, D. Kim, E.-T. Kim, Enhanced photoelectrochemical activity in the heterostructure of vertically aligned few-layer MoS2 flakes on ZnO, Electrochim. Acta 260 (2018) 150–156.
[7] B. Hinnemann, P.G. Moses, J. Bonde, K.P. Jørgensen, J.H. Nielsen, S. Horch, I. Chorkendorff, J.K. Nørskov, Biomimetic hydrogen evolution: MoS2 nanoparticles as catalyst for hydrogen evolution, J. Am. Chem. Soc. 127 (15) (2005) 5308–5309.
[8] S. Li, S. Wang, M.M. Salamone, A.W. Robertson, S. Nayak, H. Kim, S.C.E. Tsang, M. Pasta, J.H. Warner, Edge-enriched 2D MoS2 thin films grown by chemical vapor deposition for enhanced catalytic performance, ACS Catal. 7 (1) (2017) 877–886.
[9] X. Zhang, Z. Du, X. Luo, A. Sun, Z. Wu, D. Wang, Template-free fabrication of hierarchical MoS2/MoO2 nanostructures as efficient catalysts for hydrogen production, Appl. Surf. Sci. 433 (2018) 723–729.
[10] G. Zhou, X. Xu, J. Yu, B. Feng, Y. Zhang, J. Hu, Y. Zhou, Vertically aligned MoS2/MoOx heterojunction nanosheets for enhanced visible-light photocatalytic activity and photostability, CrystEngComm 16 (38) (2014) 9025–9032.
[11] X. Zhang, C. Shao, X. Li, F. Miao, K. Wang, N. Lu, Y. Liu, 3D MoS2 nanosheet/TiO2 nanofiber heterostructures with enhanced photocatalytic activity under UV irradiation, J. Alloy. Compd. 686 (2016) 137–144.
[12] V. Eyert, R. Horny, K.H. Höck, S. Horn, Embedded Peierls instability and the electronic structure of MoO2, J. Phys. Condens. Matter 12 (23) (2000) 4923–4946.
[13] Y. Zhao, Y. Zhang, Z. Yang, Y. Yan, K. Sun, Synthesis of MoS(2) and MoO(2) for their applications in H(2) generation and lithium ion batteries: a review, Sci. Technol. Adv. Mater. 14 (4) (2013) 043501-043501.
[14] D. Xiao, J. Zhang, X. Li, D. Zhao, H. Huang, J. Huang, D. Cao, Z. Li, C. Niu, Nanocarved MoS2–MoO2 hybrids fabricated using in situ grown MoS2 as nanomasks, ACS Nano 10 (10) (2016) 9509–9515.
[15] Y. Rheem, Y. Han, K.H. Lee, S.-M. Choi, N.V. Myung, Synthesis of hierarchical MoO2/MoS2 nanofibers for electrocatalytic hydrogen evolution, Nanotechnology 28 (10) (2017) 105605.
[16] J. Yan, A. Rath, H. Wang, S.H. Yu, S.J. Pennycook, D.H.C. Chua, Study of unique and highly crystalline MoS2/MoO2 nanostructures for electro chemical applications, Mater. Res. Lett. 7 (7) (2019) 275–281.
[17] M.A. Camacho-López, L. Escobar-Alarcón, M. Picquart, R. Arroyo, G. Córdoba, E. Haro-Poniatowski, Micro-Raman study of the m-MoO2 to α-MoO3 transformation induced by cw-laser irradiation, Opt. Mater. 33 (3) (2011) 480–484.
[18] F. Pedraza, J. Cruz-Reyes, D. Acosta, M.J. Yanez, M. Avalos-Borja, S. Fuentes, The structure characterization of MoS2 and WS2 catalysts by HREM, J. Phys. Condens. Matter 5 (33A) (1993) A219–A220.
[19] P.A. Spevack, N.S. McIntyre, A Raman and XPS investigation of supported molybdenum oxide thin films. 2. Reactions with hydrogen sulfide, J. Phys. Chem. 97 (42) (1993) 11031–11036.
[20] A.M. de Jong, H.J. Borg, L.J. van Ijzendoorn, V.G.F.M. Soudant, V.H.J. de Beer, J.A.R. van Veen, J.W. Niemantsverdriet, Sulfidation mechanism by molybdenum catalysts supported on silica/silicon(100) model support studied by surface spectroscopy, J. Phys. Chem. 97 (24) (1993) 6477–6483.
[21] W. Zhou, D. Hou, Y. Sang, S. Yao, J. Zhou, G. Li, L. Li, H. Liu, S. Chen, MoO2 nanobelts@nitrogen self-doped MoS2 nanosheets as effective electrocatalysts for hydrogen evolution reaction, J. Mater. Chem. A 2 (29) (2014) 11358–11364.
[22] Y. Hou, A.B. Laursen, J. Zhang, G. Zhang, Y. Zhu, X. Wang, S. Dahl, I. Chorkendorff, Layered nanojunctions for hydrogen-evolution catalysis, Angew. Chem. Int. Ed. 52 (13) (2013) 3621–3625.
[23] A. Müller, R. Jostes, W. Jaegermann, R. Bhattacharyya, Spectroscopic investigation on the molecular and electronic structure of [Mo3S13]2−, a discrete binary transition metal sulfur cluster, Inorg. Chim. Acta 41 (1980) 259–263.
[24] J.G. Choi, L.T. Thompson, XPS study of as-prepared and reduced molybdenum oxides, Appl. Surf. Sci. 93 (2) (1996) 143–149.
[25] Y. Feldman, E. Wasserman, D.J. Srolovitz, R. Tenne, High-Rate, Gas-Phase Growth of MoS < sub > 2 < /sub > Nested inorganic fullerenes and nanotubes, Science 267 (5195) (1995) 222–225.
[26] X.L. Li, Y.D. Li, Formation of MoS2 inorganic fullerenes (IFs) by the reaction of MoO3 nanobelts and S, chemistry – A, Eur. J. 9 (12) (2003) 2726–2731.
[27] X. Wang, H. Feng, Y. Wu, L. Jiao, Controlled synthesis of highly crystalline MoS2 flakes by chemical vapor deposition, J. Am. Chem. Soc. 135 (14) (2013) 5304–5307.
[28] Z. Fan, X. Huang, C. Tan, H. Zhang, Thin metal nanostructures: synthesis, properties and applications, Chem. Sci. 6 (1) (2015) 95–111.
[29] B.E. Deal, A.S. Grove, General relationship for the thermal oxidation of silicon, J. Appl. Phys. 36 (12) (1965) 3770–3778.
[30] D.-B. Seo, S. Kim, T.N. Trung, D. Kim, E.-T. Kim, Conformal growth of few-layer MoS2 flakes on closely-packed TiO2 nanowires and their enhanced photoelectrochemical reactivity, J. Alloy. Compd. 770 (2019) 686–691.